Threshold and Laser Conversion in Nanostructured-Resonator Parametric Oscillators

Haixin Liu[1,2,*] Grant M. Brodnik,[1,2] Jizhao Zang[1,2] David R. Carlson[1,3] Jennifer A. Black[1] and Scott B. Papp[1,2]

[1]*Time and Frequency Division, National Institute of Standards and Technology, Boulder, Colorado, USA*
[2]*Department of Physics, University of Colorado, Boulder, Colorado, USA*
[3]*Octave Photonics, Louisville, Colorado, USA*

We explore optical parametric oscillation (OPO) in nanophotonic resonators, enabling arbitrary, nonlinear phase matching and nearly lossless control of energy conversion. Such pristine OPO laser converters are determined by nonlinear light-matter interactions, making them both technologically flexible and broadly reconfigurable. We utilize a nanostructured inner-wall modulation in the resonator to achieve universal phase matching for OPO-laser conversion, but coherent backscattering also induces a counterpropagating pump laser. This depletes the intraresonator optical power in either direction, increasing the OPO threshold power and limiting laser-conversion efficiency, the ratio of optical power in target signal and idler frequencies to the pump. We develop an analytical model of this system that emphasizes an understanding of optimal laser-conversion and threshold behaviors, and we use the model to guide experiments with nanostructured-resonator OPO laser-conversion circuits, fully integrated on chip and unlimited by group-velocity dispersion. Our Letter demonstrates the fundamental connection between OPO laser-conversion efficiency and the resonator coupling rate, subject to the relative phase and power of counterpropagating pump fields. We achieve (40 ± 4) mW of on-chip power, corresponding to $(41 \pm 4)\%$ conversion efficiency, and discover a path toward near-unity OPO laser-conversion efficiency.

Introduction.—Optical parametric oscillation (OPO) features common behaviors in many physical systems. The intensity distribution of the optical field shows as a Turing pattern, similar to those in biological systems [1] and sand dunes [2]. These patterns arise from nonlinearity of the reaction-diffusion equation. With sand dunes there is a nonlinear surface velocity profile [3], while for nonlinear optics it is the nonlinear refractive index. Since OPO is a coherent process, it is subject to a narrow range of phase-matching solutions. Still, we can trace the coherent oscillating output of the OPO to its constituent nonlinear dynamics [4,5]. For example, accidental [6] and controllable [7–9] mode frequency shifts have been used to balance group-velocity dispersion (GVD) and Kerr shifts in microresonator OPO. Recently, photonic-crystal resonators (PhCRs) have provided a route to phase match OPO in nearly any dispersion regime, which we call universal phase matching [10]. The accessibility of these controls for nonlinear dynamics in OPO makes the system both interesting to search for novel phenomena and to understand similar dynamics in related physical systems.

OPO laser conversion also has numerous applications in engineering. Degenerate OPO works as a converter of the pump-laser frequency to a tunable signal and idler frequency, providing a coherent source with designable wavelength [11]. Microresonators further make OPO laser converters chip integrated. An intrinsic condition of OPO is phase matching, which is traditionally achieved by

designing anomalous GVD to balance Kerr frequency shifts. With GVD engineering, OPO in microresonators has been realized in silica [12,13], aluminum nitride [14], silicon nitride [15,16], and tantalum pentoxide [17] platforms. Microresonator OPO has also been explored with novel bound states in the continuum to tailor wavelength-dependent coupling conditions [18]. With PhCR OPO [10], nanostructuring the microresonator waveguide induces coherent backscattering and a controllable frequency splitting of one or more azimuthal modes. This provides direct phase matching between three modes of the device.

While tunable phase matching is important for a laser converter, the conversion efficiency (CE), defined as the ratio between the signal and idler output power and the pump laser power, is essential as well. In previous research, the highest CE of microresonator OPO with standard couplers is $< 40\%$, and the highest reported on-chip output is ≈ 20 mW [12,19–22]. In the case of PhCRs, backscattering depletes the available power available for OPO threshold and reduces conversion efficiency in a single propagation direction. Despite this, CE in PhCRs exceeding 10% has been demonstrated by operating in the overcoupled regime [10]. On the other hand, for frequency-comb generation, which has a similar operating principle as OPO [23–25], a pump-to-comb conversion efficiency as high as 83% has recently been demonstrated by placing a pump reflector to maximize the pump intensity in a PhCR [26]. However, the upper limit of OPO CE and
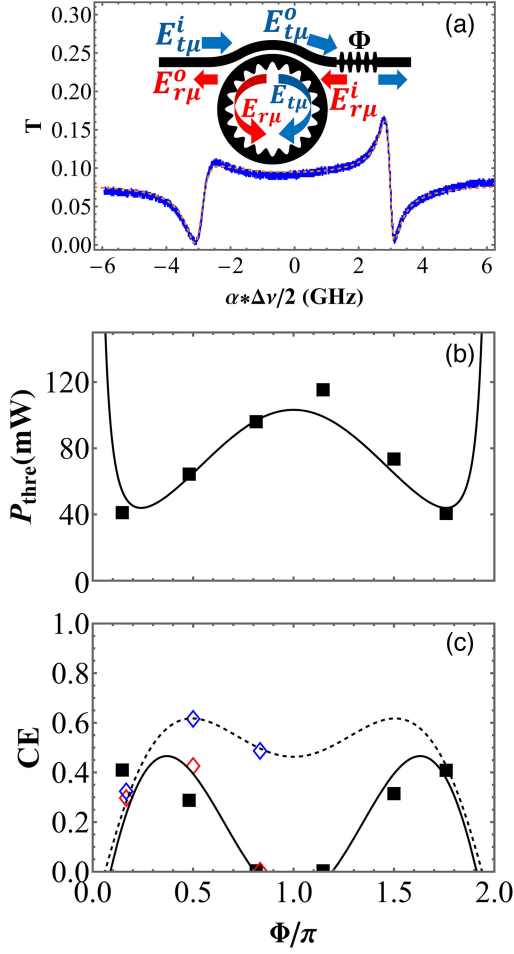
FIG. 1. Φ dependence. (a) A diagram and a transmission trace of a PhCR with pump reflector. The blue curve is the normalized transmittance from experiment. The orange dashed line plots the fit. (b) P_{thre} vs Φ with $K = 6.0 \pm 0.6$, $R = 0.8 \pm 0.1$. The solid curve shows analytic P_{thre} with $\eta = 29.7$ mW and the squares are experimental data. (c) CE vs Φ with $K = 6.0 \pm 0.6$, $R = 0.8 \pm 0.1$. The solid and dashed curve plot the analytic CE at OPhM for $F = 1.8$ and 2.3 respectively. The diamonds are the corresponding simulation results for $F = 1.8$ (red) and 2.3 (blue). Squares are experimental results with $F = 1.80 \pm 0.05$.

optimal system integration of the PhCR with pump reflector remains a research question. Moreover, a physical understanding of this system will enable future devices with access to large parametric gain for broadly reconfigurable wavelength access and the highest output power. Such chip-scale technologies would be useful for applications as diverse as optical telecommunications [27,28], spectroscopy [29], and optical sensors [30,31]. This Letter investigates the OPO CE in a PhCR with pump reflector and provides guidance for future device design.

Here, we develop an analytical framework to describe OPO laser converters with counterpropagating pump fields, and derive formulas for CE and threshold power. Moreover, we develop and implement the experimental infrastructure for an integrated PhCR with a pump reflector in the bus

waveguide. The PhCR induces coherent backscattering within the resonator, and the pump reflector transforms the pump into counterpropagating fields. Thereby, we control the phase between the counterpropagating pump fields in the bus waveguide and the backscattered pump mode inside the PhCR, suppressing the unused pump power in one direction and optimizing the utility of pump power. Our experiments systematically explore the interaction of counterpropagating pump laser fields in the PhCR. The result is in good agreement with our analytical model of the nonlinear system. By measuring the output power, the sum of the power of idler and signal in both directions, we demonstrate $(41 \pm 4)\%$ CE of OPO, defined as the ratio between the on-chip output power and the on-chip pump power. This measurement corresponds to (40 ± 4) mW on-chip output power with idler and signal at (185.06 ± 0.04) THz and (200.04 ± 0.04) THz. The corresponding spectra are in the Supplemental Material [32]. This Letter illuminates a regime of OPO in which we unleash universal phase matching and high CE through nanophotonic design, and finds a path to on-chip tunable frequency converter with low threshold and near-unity efficiency. Our theoretical model also helps understand other pump recycling laser systems such as parametric down conversion systems [33].

Theory.—The dynamics of the system depends both on the linear coupling process between the bus waveguide and the PhCR, and a nonlinear process within the PhCR. The nonlinear process is described by the normalized, modified Lugiato-Lefever equation (LLE) [34]:

$$\frac{\partial E_{t\mu}}{\partial t} = -[1 + i(\alpha + D_\mu)]E_{t\mu} + \left(F_t - i\frac{\xi}{2}E_{r\mu}\right)\delta_{\mu,0}$$

$$+ i\left(\sum_{\mu_1,\mu_2} E_{t\mu_1} E_{t\mu_2} E^*_{t(\mu_1+\mu_2-\mu)} + 2E_{t\mu}\sum_{\mu_3} I_{r\mu_3}\right)$$

$$\frac{\partial E_{r\mu}}{\partial t} = -[1 + i(\alpha + D_\mu)]E_{r\mu} + \left(F_r - i\frac{\xi}{2}E_{t\mu}\right)\delta_{\mu,0}$$

$$+ i\left(\sum_{\mu_1,\mu_2} E_{r\mu_1} E_{r\mu_2} E^*_{r(\mu_1+\mu_2-\mu)} + 2E_{r\mu}\sum_{\mu_3} I_{t\mu_3}\right). \quad (1)$$

The diagram in Fig. 1(a) shows the components of the field in our devices. The fields in the bus waveguide propagate in both transmitted and reflected directions, denoted by subscripts t and r, respectively. Superscripts i and o further denote the input and output fields relative to the PhCR in each direction. The fields in the PhCR also have two counterpropagating directions: clockwise (CW) and counterclockwise (CCW), coupling with the light transmitted and reflected in the bus waveguide, respectively. We decompose the field in each direction inside the PhCR into different modes, denoted by $E_{t\mu}$ (CW) and $E_{r\mu}$ (CCW), where μ represents the mode number relative to the pump

mode, $\mu = 0$. The field here is normalized such that the nonlinearity thresholds when $E_{t\mu}(E_{r\mu}) \sim 1$. We use $I_{t\mu} = |E_{t\mu}|^2$ or $I_{r\mu} = |E_{r\mu}|^2$ to denote the intensity of each mode. F_t and F_r are the effective driving force in each direction, $\delta_{\mu,0}$ is the Kronecker delta, α is the detuning of the pump laser, and D_μ is the integrated dispersion defined by $D_\mu = \nu_\mu - (\nu_0 + \text{FSR}\mu)$, where ν_μ is the cold cavity resonance frequency of mode μ and FSR is the free spectral range [4,10]. The interaction between CW and CCW fields induced by the nanostructured inner-wall modulation is characterized by ξ [10]. Variables α, D_μ, and ξ are normalized by the half-width of the resonator $\Delta\nu/2 = \kappa/(4\pi)$, and the time t is normalized by $2/\kappa$. The total loss rate of the ring is $\kappa = \kappa_i + \kappa_c$, where κ_i is the intrinsic loss rate and κ_c is the rate of energy exchange between the bus waveguide and the ring. The value $K = \kappa_c/\kappa_i$ is the coupling coefficient.

According to coupling theory (see Supplemental Material), for the transmitted direction, the fields input to and exiting the PhCR satisfy $E_{t\mu}^i = F_t\delta_{\mu,0}/\sqrt{r_{\text{EF}}}$ and $E_{t\mu}^o = E_{t\mu}^i - \sqrt{r_{\text{EF}}}E_{t\mu}$, respectively. $r_{\text{EF}} = 2K/(K + 1)$ is the conversion coefficient between the field in the bus waveguide and F_t or F_r, and is of the utmost importance to optimizing CE. With a perfect pump reflector that only reflects the pump frequency, the pump mode field E_{t0}^o is recycled into the CCW driving force $F_r = r(F_t - r_{\text{EF}}E_{t0}^o)$, and thus improves CE. The reflection coefficient is $r = \sqrt{R}e^{i\Phi}$, where R is the reflectivity and Φ the reflector phase. Similar to the transmitted wave, the reflected wave inside the bus waveguide satisfies $E_{r\mu}^i = F_r\delta_{\mu,0}/\sqrt{r_{\text{EF}}}$ and $E_{r\mu}^o = E_{r\mu}^i - \sqrt{r_{\text{EF}}}E_{r\mu}$.

The normalized input power equals $|E_{t0}^i|^2 = |F_t|^2/r_{\text{EF}}$. For convenience, we replace F_t with F and assume it to be a real number below. The transmitted and reflected pump-mode fields are $\sqrt{1 - |r|^2}E_{t0}^o$ and E_{r0}^o. For nonpump modes, the driving forces and the pump reflector have no effect. Therefore, the total output power of nonpump modes is $\sum_{\mu \neq 0}(|E_{t\mu}^o|^2 + |E_{r\mu}^o|^2) = r_{\text{EF}}I_c$, and $\text{CE} = r_{\text{EF}}I_c/|E_{t0}^i|^2$, where $I_c = \sum_{\mu \neq 0}(|E_{t\mu}|^2 + |E_{r\mu}|^2)$. According to the definition of K, the intrinsic loss is $P_{\text{loss}} = r_{\text{EF}}(I_{t0} + I_{r0} + I_c)/K$. For the steady state, due to energy conservation,

$$|E_{t0}^i|^2 = \left|\sqrt{1 - |r|^2}E_{t0}^o\right|^2 + |E_{r0}^o|^2 + r_{\text{EF}}I_c + P_{\text{loss}}. \quad (2)$$

Replacing $E_{t0}^i, E_{t0}^o, E_{r0}^o$ with E_{t0}, E_{r0}, and F, and solving I_c, we obtain

$$\text{CE} = r_{\text{EF}}^2 \frac{F\text{Re}[E_{t0} + r^*E_{r0}] - I_{t0} - I_{r0} - r_{\text{EF}}\text{Re}[rE_{t0}E_{r0}^*]}{F^2}. \quad (3)$$

We further simplify the formula above for some specific cases. For an ordinary resonator without pump reflector, $E_{r0} = 0$ and Eq. (3) becomes $\text{CE} = r_{\text{EF}}^2(\text{Re}[E_{t0}]/F - I_{t0}/F^2)$ [19,35]. However, PhCRs are quite different. For wide span OPO with normal GVD, phase matching requires $\xi \gg 1$, which we call the large mode split approximation. The strong interaction between the CW and CCW wave of the pump mode establishes coherence between them: $E_{t0} \approx -E_{r0}$ for the red-shifted resonance mode ($\alpha > 0$); see Supplemental Material. According to Eq. (3), a smaller I_{t0} enables the same CE with smaller F. When OPO exists, I_{t0} is determined by the phase-matching condition [19]. For ordinary rings, the phase matching is determined by D_μ only. However, in PhCRs, the effect of D_μ on phase matching can be compensated by ξ. When $I_{t0} = 1$ and E_{t0} have the same complex angle as $1 - r$, CE is largest. This is satisfied by optimizing ξ and sweeping α, which we call optimal phase matching (OPhM); see Supplemental Material. At OPhM and $\xi \gg 1$, Eq. (3) reduces to

$$\text{CE} = r_{\text{EF}}^2\left(\frac{1}{F}|1 - r| - \frac{1}{F^2}(2 - r_{\text{EF}}\text{Re}[r])\right). \quad (4)$$

Further, F at threshold is the solution of $\text{CE} = 0$:

$$F_{\text{thre}} = \frac{2 - r_{\text{EF}}\text{Re}[r]}{|1 - r|}. \quad (5)$$

The actual input power P in experiment can be written as $P = \eta F^2$, where η originates from the normalization of the modified LLE [Eq. (1)], and depends on the half-width of the resonator, the linear and nonlinear refractive index of the PhCR, and the mode volume [36]. However, without calculating η, we can control F through P based on Eq. (5) and the threshold power P_{thre} measured in the experiment:

$$F = F_{\text{thre}}\sqrt{\frac{P}{P_{\text{thre}}}} \quad (6)$$

Equation (4) depends on four variables: F, Φ, R, and K (included in r_{EF}). The maximum of CE happens at $F = 2F_{\text{thre}}$ (namely $P = 4P_{\text{thre}}$), which we call saturation CE and denote by CE_{sat},

$$\text{CE}_{\text{sat}} = \frac{r_{\text{EF}}^2}{4}\frac{|1 - r|^2}{2 - r_{\text{EF}}\text{Re}[r]}. \quad (7)$$

For a PhCR without a pump reflector, $F_{\text{thre}} = 2$ and $\text{CE}_{\text{sat}} = [K/(K + 1)]^2/2$. For a fixed R, $F_{\text{thre}} < 2$ at some Φ, and CE_{sat} is maximized when $\Phi = \pi$. The maximum of CE_{sat} is $K^2/[(K + 1)(K + 1/2)]$ when $r = -1$, which is greater than the CE limit of ordinary resonators $[K/(K + 1)]^2$ [19].
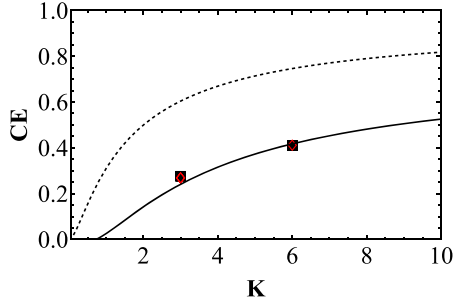
FIG. 2. K dependence. The solid curve is analytic CE at OPhM with $F = 1.85$, $\Phi = 1.715\pi$, $R = 0.8$. The dashed curve is the analytic saturation CE with $\Phi = \pi$, $R = 0.8$. The squares are experimental results with approximately same condition. The red diamonds are the simulation results with the same parameters.

Experiment.—We explore and measure OPO laser converters with a PhCR and a pump reflector, demonstrating the close connection between lasers we implement with integrated photonics and our predictive model of the system. Figure 1 presents the foundations of our system, including the Φ dependence of threshold power and CE. The pump reflector is a series of waveguide-width modulations with tapering period and amplitude that controls the width and the location of the reflection band [37]. The PhCR enables deterministic single-mode splitting by periodically modulating the resonator inner wall with a nanostructured period that determines the split resonance wave vector. The amplitude of the modulation is proportional to ξ [10]. We implement the PhCR with pump reflector in the tantala integrated photonics platform developed by us [17,38]. The pump laser is a tunable continuous wave laser amplified with an erbium-doped fiber. More details of fabrication and experimental testing are in Supplemental Material.

To test our analytic model, we compare the results with experiment and numerical simulation, using Eq. (1) (see Supplemental Material). The measured pump reflectivity varies from 72% to 83% due to the uncertainty of the measurement and the tolerance of fabrication between different chips. In each plot, we tested the devices with similar Rs and use their average R in the analytic curves and simulations. By rotating the nanostructured inner-wall resonator modulation, we equivalently change the relative phase Φ between reflected light in the bus waveguide and the field inside the PhCR. We measure Φ as well as K and ξ by fitting the transmission, T; see Fig. 1(a) and Supplemental Material. Figure 1(b) shows the Φ dependent measurement of P_{thre} [black squares; Fig. 1(b)], which is consistent with Eq. (5) [solid curve; Fig. 1(b)] after fitting the conversion coefficient, $\eta = 29.7$ mW.

Figure 1(c) shows the Φ dependent measurement of CE [black squares; Fig. 1(c)]. We control F to 1.80 ± 0.05 by comparing the input power with P_{thre} for each device, according to Eq. (6). We calculate CE from the inferred on-chip output and input power, with an uncertainty of 0.4 dB.
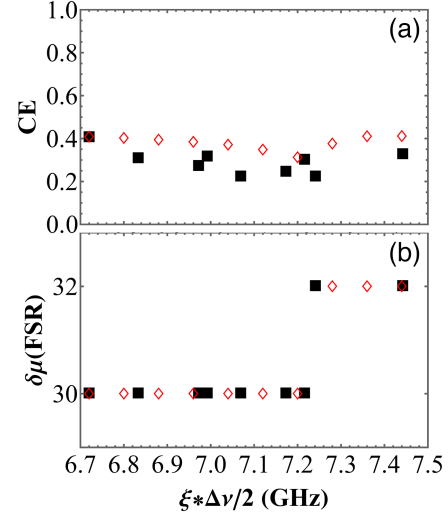
FIG. 3. ξ dependence. (a),(b) CE vs ξ and $\delta\mu$ vs ξ. The black squares are the experiment results and the red diamonds are the simulation results.

The solid and dashed curves are the analytic CE [Eq. (4)] at OPhM with $F = 1.8$ and 2.3 respectively. We also performed a numerical simulation based on Eq. (1) to verify our analytic CE formula [red ($F = 1.8$) and blue ($F = 2.3$) diamonds in Fig. 1(c)]. Both simulation and experimental results match our analytical CE model well. Figure 1 demonstrates that the sensitive CE dependence on Φ. Although the device with $\Phi = \pi$ reflector has the maximum saturation CE, for small input power, the devices with reflectors of other phases achieved higher CE first due to lower F_{thre}.

As discussed above, the coupling coefficient K is critical to CE. We change this parameter by adjusting the gap between the bus waveguide and the PhCR; see Supplemental Material. Figure 2 shows the dependence of CE on K. The solid curve plots the analytic CE at OPhM with $F = 1.85$, $\Phi = 1.715\pi$, and $R = 0.8$. The black squares are the experimental results and the red diamonds are the simulation results with the same parameters obtained from the modified LLE Eq. (1). The results are nearly overlapping, demonstrating the validity of the derived analytic expressions. The dashed curve is the analytic CE_{sat} with the same reflectivity but optimal phase $\Phi = \pi$. It shows that even without modification on the reflector structure, CE can reach nearly 80% with $K = 6$ when Φ is optimized and the input power is increased to saturation, $P = 4P_{\text{thre}}$. In addition, according to Eq. (7), with an ideal reflectivity $R = 100\%$, CE can reach the theoretical upper boundary $K^2/[(K + 1)(K + 1/2)]$, which asymptotically approaches unity when $K \to +\infty$.

Our simplified CE formula [Eq. (4)] is valid only when OPhM is satisfied. In order to achieve OPhM, we sweep ξ by adjusting the modulation amplitude of the PhCR's nanostructured inner wall. Figure 3(a) shows the CE dependence
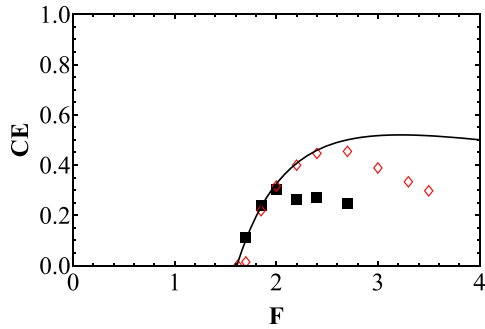
FIG. 4. F dependence. CE vs F. The solid curve and red diamonds shows the analytic CE and simulation results with $R = 0.72$, $\Phi = 1.372\pi$, $K = 2.8$, respectively. The black squares are experiment results with $R = 0.7 \pm 0.1$, $\Phi = (1.36 \pm 0.05)\pi$, $K = 2.8 \pm 0.3$.

of ξ with all other parameters fixed. We find CE spans $\approx 20\%$–40%, where the experimental results (black squares) are in good agreement with our numerical simulation based on Eq. (1) (red diamonds). The small decrease in CE corresponds to a change in the generated signal and idler frequencies, whose span in FSR is $\delta\mu$, as seen in Fig. 3(b), and suggest that a new pair of PhCR modes achieves phase matching.

We also investigate the dependence of CE on F, the pump driving field, which is controlled by the input pump power. Our results are summarized in Fig. 4. The solid curve and red diamonds are the analytic CE [Eq. (4)] and simulation results at OPhM with $R = 0.72$, $\Phi = 1.372\pi$, $K = 2.8$. The black squares are experimental results with $R = 0.7 \pm 0.1$, $\Phi = (1.36 \pm 0.05)\pi$, $K = 2.8 \pm 0.3$. The results are consistent at small F, but diverge at larger F. We attribute this divergence to two reasons. First, our theoretical model Eq. (4) is limited to the OPO case, which assumes that only the pump, idler, and signal modes have nonzero intensity. When F is large, more than one pair of modes can achieve phase matching, which we call cascade, and decentralize the pump mode power. This is no longer an OPO process and therefore not covered by our analytic prediction. However, our simulations do predict such cascade and thus diverge from the analytic curve. Second, the imperfect environment in the experiment is not fully described by either our analytical model or numerical simulation. For example, the reflectors in our devices have some reflectivity at the signal and idler modes and K at the idler mode is larger than at the pump and signal modes. When CE is high, reflected idler light may excite other four-wave mixing processes, further decentralizing the pump mode power. The reflectivity on the signal and idler can be reduced with an optimized reflector, and the wavelength dependence of K can be optimized by engineering of the coupler. Moreover, cascade can be avoided by utilizing other dispersion regimes and values of ξ, or operating with a larger FSR.

In this Letter, we show that a pump reflector can reduce OPO threshold power and increase CE by controlling the coupling of counterpropagating pump lasers in PhCR. We develop a theory to explain this mechanism and derive analytic formulas of CE and threshold power for nano-structured-resonator OPO. Our analytical model has been systematically verified in our experiments and we have obtained $(41 \pm 4)\%$ CE and (40 ± 4) mW on-chip power for OPO laser conversion. Higher CE is limited by the nonideal reflector spectrum and cascade in our experiment. Through nanophotonic design, we highlight a regime of OPO with high CE and universal phase matching and realize a robust laser platform. Our pump reflector approach also applies to parametric down-conversion or other laser-conversion systems.

*Corresponding author: haixin.liu@colorado.edu

[1] D. Bullara and Y. De Decker, Pigment cell movement is not required for generation of turing patterns in zebrafish skin, Nat. Commun. **6**, 6971 (2015).

[2] K. Kroy, G. Sauermann, and H. J. Herrmann, Minimal model for sand dunes, Phys. Rev. Lett. **88**, 054301 (2002).

[3] Y. Amarouchene, J. F. Boudet, and H. Kellay, Dynamic sand dunes, Phys. Rev. Lett. **86**, 4286 (2001).

[4] T. J. Kippenberg, A. L. Gaeta, M. Lipson, and M. L. Gorodetsky, Dissipative Kerr solitons in optical micro-resonators, Science **361**, eaan8083 (2018).

[5] S.-P. Yu, D. C. Cole, H. Jung, G. T. Moille, K. Srinivasan, and S. B. Papp, Spontaneous pulse formation in edgeless photonic crystal resonators, Nat. Photonics **15**, 461 (2021).

[6] X. Xue, Y. Xuan, Y. Liu, P.-H. Wang, S. Chen, J. Wang, D. E. Leaird, M. Qi, and A. M. Weiner, Mode-locked dark pulse Kerr combs in normal-dispersion microresonators, Nat. Photonics **9**, 594 (2015).

[7] X. Lu, S. Rogers, W. C. Jiang, and Q. Lin, Selective engineering of cavity resonance for frequency matching in optical parametric processes, Appl. Phys. Lett. **105**, 151104 (2014).

[8] X. Xue, Y. Xuan, P.-H. Wang, Y. Liu, D. E. Leaird, M. Qi, and A. M. Weiner, Normal-dispersion microcombs enabled by controllable mode interactions, Laser Photonics Rev. **9**, L23 (2015).

[9] S. A. Miller, Y. Okawachi, S. Ramelow, K. Luke, A. Dutt, A. Farsi, A. L. Gaeta, and M. Lipson, Tunable frequency

combs based on dual microring resonators, Opt. Express 23, 21527 (2015).

[10] J. A. Black, G. Brodnik, H. Liu, S.-P. Yu, D. R. Carlson, J. Zang, T. C. Briles, and S. B. Papp, Optical-parametric oscillation in photonic-crystal ring resonators, Optica 9, 1183 (2022).

[11] X. Lu, G. Moille, A. Singh, Q. Li, D. A. Westly, A. Rao, S.-P. Yu, T. C. Briles, S. B. Papp, and K. Srinivasan, Milliwatt-threshold visible–telecom optical parametric oscillation using silicon nanophotonics, Optica 6, 1535 (2019).

[12] T. J. Kippenberg, S. M. Spillane, and K. J. Vahala, Kerr-nonlinearity optical parametric oscillation in an ultrahigh-q toroid microcavity, Phys. Rev. Lett. 93, 083904 (2004).

[13] N. L. B. Sayson, K. E. Webb, S. Coen, M. Erkintalo, and S. G. Murdoch, Widely tunable optical parametric oscillation in a Kerr microresonator, Opt. Lett. 42, 5190 (2017).

[14] Y. Tang, Z. Gong, X. Liu, and H. X. Tang, Widely separated optical Kerr parametric oscillation in AlN microrings, Opt. Lett. 45, 1124 (2020).

[15] X. Lu, G. Moille, A. Rao, D. A. Westly, and K. Srinivasan, On-chip optical parametric oscillation into the visible: Generating Red, Orange, Yellow, and Green from a near-infrared pump, Optica 7, 1417 (2020).

[16] R. R. Domeneguetti, Y. Zhao, X. Ji, M. Martinelli, M. Lipson, A. L. Gaeta, and P. Nussenzveig, Parametric sideband generation in cmos-compatible oscillators from visible to telecom wavelengths, Optica 8, 316 (2021).

[17] H. Jung, S.-P. Yu, D. R. Carlson, T. E. Drake, T. C. Briles, and S. B. Papp, Tantala Kerr nonlinear integrated photonics, Optica 8, 811 (2021).

[18] F. Lei, Z. Ye, K. Twayana, Y. Gao, M. Girardi, Ó. B. Helgason, P. Zhao, and V. Torres-Company, Hyperparametric oscillation via bound states in the continuum, Phys. Rev. Lett. 130, 093801 (2023).

[19] N. L. B. Sayson, T. Bi, V. Ng, H. Pham, L. S. Trainor, H. G. Schwefel, S. Coen, M. Erkintalo, and S. G. Murdoch, Octave-spanning tunable parametric oscillation in crystalline Kerr microresonators, Nat. Photonics 13, 701 (2019).

[20] F. Zhou, X. Lu, A. Rao, J. Stone, G. Moille, E. Perez, D. Westly, and K. Srinivasan, Hybrid-mode-family Kerr optical parametric oscillation for robust coherent light generation on chip, Laser Photonics Rev. 16, 2100582 (2022).

[21] J. R. Stone, X. Lu, G. Moille, and K. Srinivasan, Efficient chip-based optical parametric oscillators from 590 to 1150 nm, APL Photonics 7, 121301 (2022).

[22] E. F. Perez, G. Moille, X. Lu, J. Stone, F. Zhou, and K. Srinivasan, High-performance Kerr microresonator optical parametric oscillator on a silicon chip, Nat. Commun. 14, 242 (2023).

[23] A. Coillet, I. Balakireva, R. Henriet, K. Saleh, L. Larger, J. M. Dudley, C. R. Menyuk, and Y. K. Chembo, Azimuthal turing patterns, bright and dark cavity solitons in Kerr combs generated with whispering-gallery-mode resonators, IEEE Photonics J. 5, 6100409 (2013).

[24] A. Pasquazi, M. Peccianti, L. Razzari, D. J. Moss, S. Coen, M. Erkintalo, Y. K. Chembo, T. Hansson, S. Wabnitz, P. Del'Haye et al., Micro-combs: A novel generation of optical sources, Phys. Rep. 729, 1 (2018).

[25] S.-P. Yu, E. Lucas, J. Zang, and S. B. Papp, A continuum of bright and dark-pulse states in a photonic-crystal resonator, Nat. Commun. 13, 3134 (2022).

[26] J. Zang, S.-P. Yu, D. R. Carlson, T. C. Briles, and S. B. Papp, Near unit efficiency in microresonator combs, in CLEO: Science and Innovations (Optica Publishing Group, Washington, 2022), pp. STh4F–3.

[27] A. Fülöp, M. Mazur, A. Lorences-Riesgo, Ó. B. Helgason, P.-H. Wang, Y. Xuan, D. E. Leaird, M. Qi, P. A. Andrekson, A. M. Weiner et al., High-order coherent communications using mode-locked dark-pulse Kerr combs from micro-resonators, Nat. Commun. 9, 1598 (2018).

[28] G. M. Brodnik, M. W. Harrington, J. H. Dallyn, D. Bose, W. Zhang, L. Stern, P. A. Morton, R. O. Behunin, S. B. Papp, and D. J. Blumenthal, Optically synchronized fibre links using spectrally pure chip-scale lasers, Nat. Photonics 15, 588 (2021).

[29] M.-G. Suh, Q.-F. Yang, K. Y. Yang, X. Yi, and K. J. Vahala, Microresonator soliton dual-comb spectroscopy, Science 354, 600 (2016).

[30] Y.-H. Lai, M.-G. Suh, Y.-K. Lu, B. Shen, Q.-F. Yang, H. Wang, J. Li, S. H. Lee, K. Y. Yang, and K. Vahala, Earth rotation measured by a chip-scale ring laser gyroscope, Nat. Photonics 14, 345 (2020).

[31] C. Bao, Z. Yuan, L. Wu, M.-G. Suh, H. Wang, Q. Lin, and K. J. Vahala, Architecture for microcomb-based Ghz-mid-infrared dual-comb spectroscopy, Nat. Commun. 12, 6573 (2021).

[32] See Supplemental Material at http://link.aps.org/supplemental/10.1103/PhysRevLett.132.023801 for details of experiment, mathematical derivation, and simulation method.

[33] S. Yang, R. Eckardt, and R. Byer, Continuous-wave singly resonant optical parametric oscillator pumped by a single-frequency resonantly doubled ND: Yag laser, Opt. Lett. 18, 971 (1993).

[34] D. V. Skryabin, Hierarchy of coupled mode and envelope models for bi-directional microresonators with Kerr non-linearity, OSA Continuum 3, 1364 (2020).

[35] J. R. Stone, G. Moille, X. Lu, and K. Srinivasan, Conversion efficiency in Kerr-microresonator optical parametric oscillators: From three modes to many modes, Phys. Rev. Appl. 17, 024038 (2022).

[36] T. C. Briles, S.-P. Yu, T. E. Drake, J. R. Stone, and S. B. Papp, Generating octave-bandwidth soliton frequency combs with compact low-power semiconductor lasers, Phys. Rev. Appl. 14, 014006 (2020).

[37] S.-P. Yu, H. Jung, T. C. Briles, K. Srinivasan, and S. B. Papp, Photonic-crystal-reflector nanoresonators for Kerr-frequency combs, ACS Photonics 6, 2083 (2019).

[38] J. A. Black, R. Streater, K. F. Lamee, D. R. Carlson, S.-P. Yu, and S. B. Papp, Group-velocity-dispersion engineering of tantala integrated photonics, Opt. Lett. 46, 817 (2021).